Nuclear Instruments and Methods in Physics Research A292 (1990) 81–96
North-Holland

DESIGN AND PERFORMANCE OF THE SAPHIR LEAD-GLASS CALORIMETER

H. BAUMEISTER, P. BECKMANN, F. BERGER, N. BRUMMUND, G. CLEWING, L. DRAGON, R. GLASOW, D. GRZONKA, W. HASSENMEIER, K.H. KAMPERT, H. LÖHNER *, T. PEITZMANN, M. PURSCHKE, R. SANTO, W. VERHOEVEN and R. WIENKE

Westfälische Wilhelms-Universität, Institut für Kernphysik, Wilhelm-Klemm-Strasse 9, D-4400 Münster, FRG

The CERN-SPS WA80 Collaboration

CERN, Geneva, Switzerland

Received 19 December 1989 and in revised form 19 January 1990

For the WA80 fixed-target heavy-ion experiment at the CERN-SPS, a 1278 element lead-glass calorimeter has been constructed to measure photons in the energy range from 0.2 to 20 GeV. We describe the design of the detector, the achieved energy and position resolution, the gain monitoring system and the performance of the high-energy photon trigger. The quality of photon identification and π^0 invariant mass reconstruction is discussed.

1. Introduction

The study of heavy-ion collisions at ultrarelativistic energies was started in late 1986 when a new heavy-ion source came into operation at the CERN-SPS, allowing to inject and accelerate oxygen nuclei and thus to expand the available beam kinetic energy by nearly two orders of magnitude as compared to Berkeley BEVALAC energies. Several experimental groups [1] have studied interactions of oxygen and sulphur beams with heavy target nuclei and investigated global event features [2–4], as well as various signals predicted for the existence of the postulated quark-gluon plasma (QGP) state [5]. One of the suggested signals of the QGP is the excess production of direct photons in the hot plasma phase [6]. However, the measurement of direct photons must cope with the large number of photons originating from the decay of neutral mesons (mainly π^0 and η) as well as with the high charged-particle multiplicity observed in central interactions. For this purpose, a detector with high π^0 and η reconstruction capability is required. The transverse-momentum distributions of π^0 and η mesons are considered to be interesting observables by themselves for probing thermodynamical and hydrodynamical properties of highly compressed nuclear matter [7,8].

The finely granulated lead-glass calorimeter SAPHIR *, which covers about 1/6 of the azimuthal ring in the pseudorapidity range from 1.5 to 2.1 in the present WA80 experimental setup [9], was therefore designed to measure photons in the energy range from 0.2 to 20 GeV and to identify π^0's and η's by their decay photons. The efficiency and accuracy of neutral meson detection will determine the detection limits of the direct photon signal.

2. Design and construction

2.1. Module design

The SAPHIR detector consists of 1278 SF5 lead-glass blocks manufactured by Schott (Mainz, FRG) of 35×35 mm^2 cross section and 460 mm length (fig. 1), corresponding to about 18 radiation lengths ($X_0 = 2.551$ cm). The transverse block dimension of 35 mm was chosen according to the experience gained from the GAMS detector system [10], so that electromagnetic showers of 10 GeV deposit $> 97\%$ of their energy within a transverse region of 3×3 blocks. Finer segmentation results in only very little improvement of position resolution, but deteriorates the energy resolution and increases the cost of the apparatus. Each block is wrapped in a double layer of 10 μm aluminum-coated mylar foil in

* Present address: KVI Groningen, 9747 AA, Groningen, The Netherlands.

* Single Arm Photondetector for Heavy Ion Reactions.

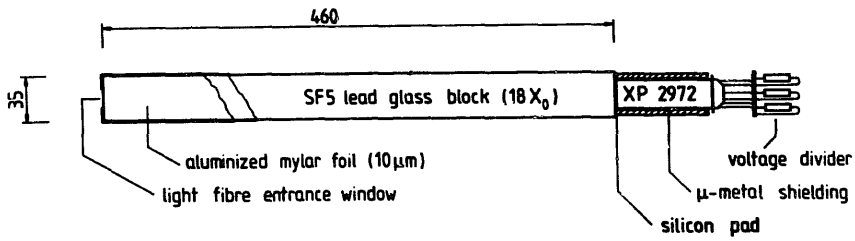

Fig. 1. Sketch of a lead-glass module with the photomultiplier and the mylar foil wrapping.

order to prevent optical cross talk, and is equipped with a ten-stage VALVO XP2972PB [11] photomultiplier (PM) mounted in a black plastic housing which is glued to the rear face of the block. The passive voltage divider is mounted on a 32 × 32 mm^2 printed circuit board with connectors directly soldered to the PM connector pins. A fast signal for trigger purposes is deduced from the ninth dynode stage via an rf transformer. The photomultiplier is covered by a 0.3 mm layer of antimagnetic sheet metal. The light coupling to the lead glass is improved by a 3 mm thick silicone pad.

2.2. Detector assembly

The detector modules are stacked in a rectangular 49 × 28 array with an overall size of 1715 × 980 mm^2. A sketch of the mechanical arrangement is given in fig. 2. Tolerances in the module size have been kept below 0.6 mm in length and 0.2 mm in the transverse dimensions. This requirement ensures mechanical stability and limits the maximum deviation of the actual module position from the expected matrix position to less than 1 mm. The lead-glass modules are vertically aligned by means

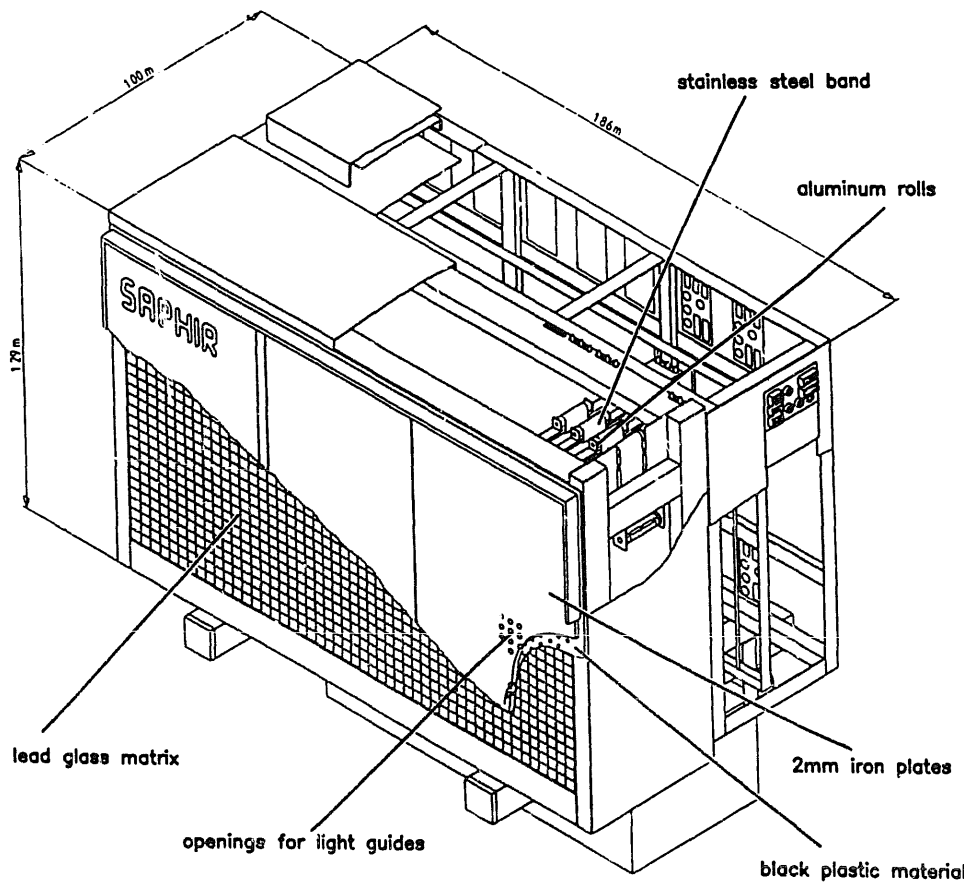

Fig. 2. Mechanical arrangement of the SAPHIR lead-glass calorimeter.

of a 0.2 mm thick and 120 mm wide stainless-steel band running vertically through the lead-glass matrix row by row. The band is guided on top and bottom of the detector by aluminum rolls and put under stress by moving and fixing these rolls in vertical direction. An additional support against sliding is achieved by steel rods running vertically through small grooves in the plastic PM housing. This is particularly important when the detector is tilted by up to 12°.

The cooling of the densely packed PM voltage dividers, which consume a total power of 2 kW, is achieved by eight fans at the bottom of the detector housing which limits the temperature difference to $< 10\,^{\circ}C$ compared to the outside environment. While the lead-glass arrangement itself is completely surrounded by black plastic material in order to ensure light tightness, the outer detector housing is made of 2 mm iron plates in order to provide shielding against outside rf noise and external magnetic fields close to the experiment. This housing also contains the light fibres for optical monitoring of the lead glass and the coaxial cables connecting the voltage dividers to multi-pin connectors on the rear detector surface.

3. The optical gain monitoring system

A distribution of the gain drifts for all 1278 phototubes measured from two consecutive runs ($\approx$ 30 min) and after 36 h is shown in fig. 3a and 3b, respectively. To be able to correct for these gain drifts and to maintain the absolute energy calibration, a reliable gain monitoring system is mandatory. We aimed for absolute and relative stability below 1%. This goal was achieved by the laser-based reference system depicted in fig. 4.

In brief, the laser light is distributed to each individual photomultiplier and is simultaneously monitored by three reference photomultipliers, whose gain is in turn monitored by ^{241}Am-doped NaI(Tl) light pulsers [12] which serve as light standards.

The intense ultraviolet light (337 nm) from the nitrogen laser [13] is widened by an inverted Galilei telescope and converted to blue light (420 nm) in a 3 mm thick wavelength shifter plate (bis-MSB) in order to match the spectral sensitivity of the photocathodes. The wavelength shifter is glued in front of a $50 \times 50 \times 460$ mm^3 plexiglas block which serves as a light mixer. The homogenized blue light is then coupled into 1300 light fibres which transmit the light to the front face of each lead-glass module. The other end of the PCS200 quartz fibres [14] with a core diameter of 200 μm and a length of 4 m are glued into cylindrical black plastic plugs which in turn fit into holes of a 10 mm thick black PVC plastic front cover plate of SAPHIR. The fibre plugs define a reproducible distance of about 2 mm between the fibre end and the lead glass. The nitrogen laser is located outside the experimental area and thus accessible for maintenance during running periods. Its light is fed via a 19 m long PCS1000 [14] quartz fibre (1 mm core diameter) to the light distribution box below the detector. A second fibre of the same type is mounted after a laser beam splitter and is used to trigger the start detectors of the experiment. The relative length of the two light fibres is adjusted to simulate the timing of beam particles traveling down the beam line, thus allowing careful gate settings and trigger tuning without requiring a particle beam.

In order to monitor the variation of the laser light intensity, three of the 1300 light fibres are fed to the three reference photomultipliers, Ref$_i$(i = 1, 2, 3), which

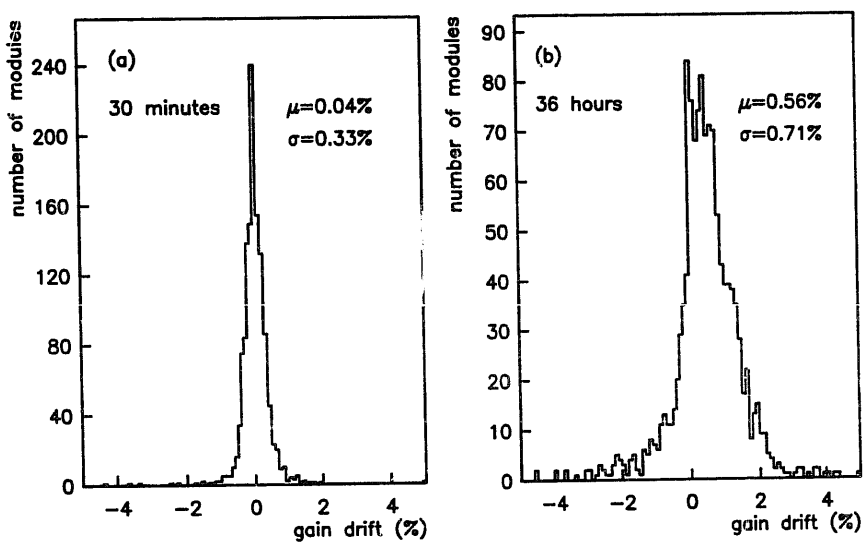

Fig. 3. Distribution of gain drifts for all SAPHIR photomultiplier tubes from two consecutive runs (a) and after 36 h (b).

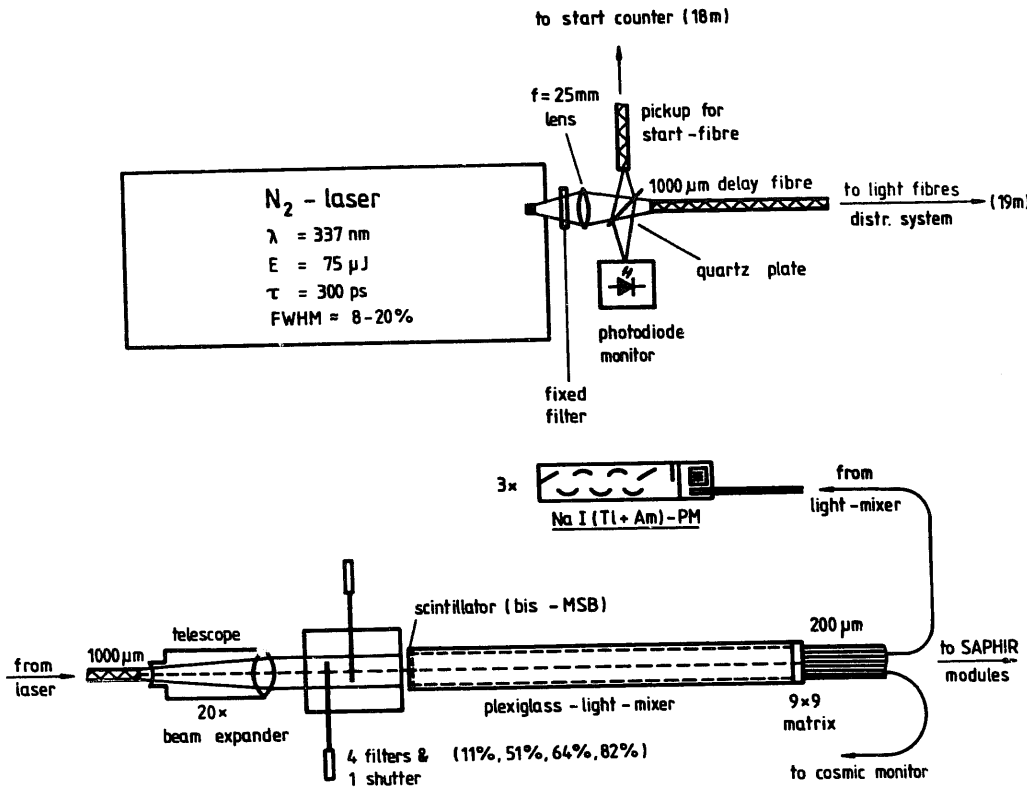

Fig. 4. Arrangement of the SAPHIR laser reference system.

independently compare the integrated charge $Q^{\text{laser}}_{\text{Ref},i}$ generated by the laser light to the charge $Q^{\text{NaI}}_{\text{Ref},i}$ produced by the scintillation light of the ^{241}Am-doped NaI(Tl) crystals. Using this triple reference system we are able to monitor the short-term variations of the phototube gains with an accuracy better than 0.5%. This result is deduced from the double ratios

$$R_{ij} = Q^{\text{laser}}_{\text{Ref},i} Q^{\text{NaI}}_{\text{Ref},j} / \left(Q^{\text{laser}}_{\text{Ref},j} Q^{\text{NaI}}_{\text{Ref},i} \right), \qquad (1)$$

which are expected to be independent of the absolute laser light intensity and of the phototube gains in the reference system. Three independent ratios of this type

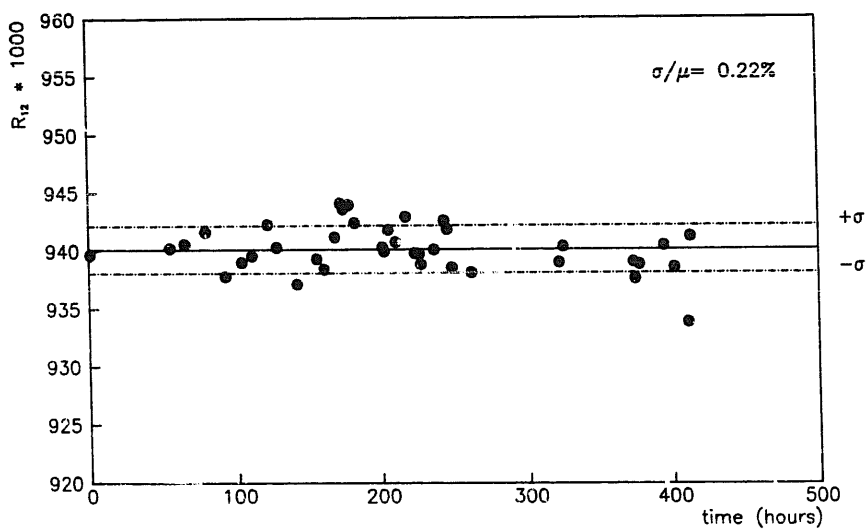

Fig. 5. Double ratios R_{12} of the reference photomultiplier signals as a function of time showing the absolute stability of the reference system.

can be determined for i, $j = 1$, 2, 3 and $i \neq j$. An example of this double ratio as a function of time is shown in fig. 5 for $i = 1$ and $j = 2$. It is found to be stable within $\sigma/\mu = 0.22\%$ for a period of 420 h. Since NaI crystals are known to get deteriorated on a time scale of several months by radiation damage and water admission [15], an additional cosmic-ray monitor is used to provide long-term gain stability by comparing the laser light (Q_C^{laser}) with the signal of minimum ionizing cosmic muons (Q_C^{muons}) passing through a thick lead-glass Cherenkov counter. The trajectory of the selected muons is defined by requiring a coincidence in four scintillator paddles. A 10 cm thick lead block is used to discriminate against soft muons and electrons interacting in the lead glass. The additional information provided by the energy signal of the minimum ionizing muons allows to define another set of reference numbers to check the stability of the NaI(Tl) light pulsers, namely the double ratios

$$R_{Ci} = Q_C^{laser} Q_{Ref,i}^{NaI} / \left(Q_{Ref,i}^{laser} Q_C^{muons} \right), \qquad (2)$$

for each of the three reference tubes $i = 1$, 2, 3. The signals of minimum ionizing muons in the cosmic-ray detector and of the NaI(Tl) light pulser in Ref_2 are shown in fig. 6a and 6b, respectively, whereas fig. 6c displays the distribution of the ratio of the laser pulses in both detectors. The double ratio R_{C1} shows a decrease from 1456.3 ± 12.0 (October 1987) to 1446.7 ± 7.1 (February 1988). This indicates a slight decrease in light yield of the NaI crystal during a period of four months.

A second aim of the laser calibration system is the linearization of the 1278 PM tubes. Therefore the laser

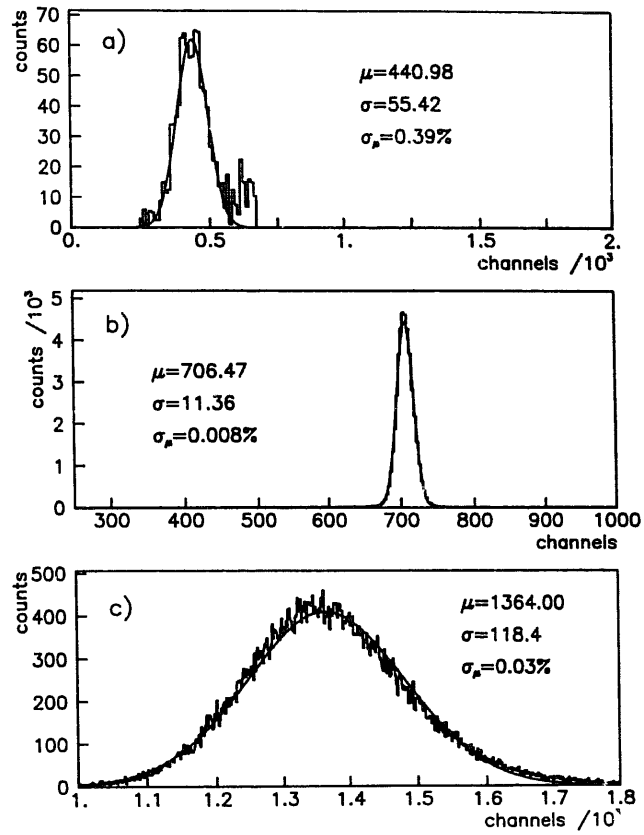

Fig. 6. Response of the reference detector Ref_2 and the cosmic ray detector: Energy spectrum of cosmic muons (a), energy spectrum of the NaI light pulser (b), event-by-event ratio of laser pulses in the cosmic and Ref_2 detector (c). The mean value μ and the standard deviation σ of the respective peaks are indicated as well as the square root of the variance of μ, σ_μ.

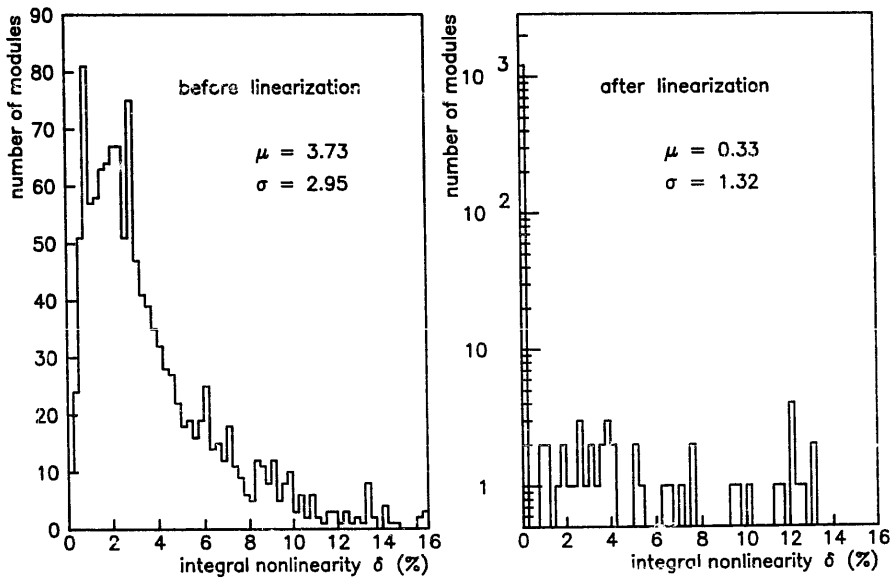

Fig. 7. Integral nonlinearity δ for all SAPHIR modules before and after applying the linearization procedure.

light intensity can be varied by a set of neutral density filters with 11.4, 51.3, 63.7 and 82.3% transmission at 337 nm which can be moved into the light path between the telescope and the wavelength shifter. Different combinations of filter settings are used to measure the linearity of the photomultiplier response over a large dynamic range. The signal $Q_{\mathrm{Ref}}^{\mathrm{laser}}$ of the laser in one reference tube is used as a measure of the laser light intensity and is plotted against the laser signal in each SAPHIR module. The obtained curves were fitted by a set of orthogonal polynomials $T_p(Q_{\mathrm{Ref}}^{\mathrm{laser}})$ with the coefficients A_p. From the polynomial fit up to the tenth order $\Sigma_{p=0}^{9} A_p T_p(Q_{\mathrm{Ref}}^{\mathrm{laser}})$, derived by the method of least squares, we deduced a correction function which is used for the subsequent linearization of each of the SAPHIR multipliers. The distribution of the integral nonlinearities, δ, of all modules before and after the linearization is shown in fig. 7, where δ is defined as the maximum value of $\delta(Q_{\mathrm{Ref}}^{\mathrm{laser}})$:

$$\delta\left(Q_{\mathrm{Ref}}^{\mathrm{laser}}\right) = \frac{\left|\left\{\sum_{p=2}^{9} A_p T_p\left(Q_{\mathrm{Ref}}^{\mathrm{laser}}\right)\right\}\right|}{\left|\left\{\sum_{p=0}^{1} A_p T_p\left(Q_{\mathrm{Ref}}^{\mathrm{laser}}\right)\right\}\right|}. \qquad (3)$$

After this linearization procedure, only 63 out of 1278 modules still showed a significant deviation from linearity which could be corrected for by an individual determination of the correction function. The linearity of the reference tubes can be checked with the help of a photodiode located at the beam splitter in front of the filter set. If the photodiode is assumed to be linear, it is possible to linearize the response functions of the reference tubes also. Due to a poor photodiode resolution (8.7%) it was merely possible to estimate the maximum nonlinearity δ of Ref_2 to be less than 1% over the full dynamic range.

4. Calibration and resolution

A detector depth of 18 radiation lengths was chosen in order to provide a containment of more than 98% of an electromagnetic shower up to 30 GeV, so that shower leakage is expected to have negligible influence on the energy resolution. On the other hand, the length of the lead-glass modules does not lead to a too large Cherenkov light absorption. Thus the energy resolution is mainly due to statistical fluctuations in the detection process.

Measurements with electron beams have been performed at DESY with a prototype detector and at the X1-beamline at the CERN-SPS with the fully assembled SAPHIR. At X1, each lead-glass module was calibrated

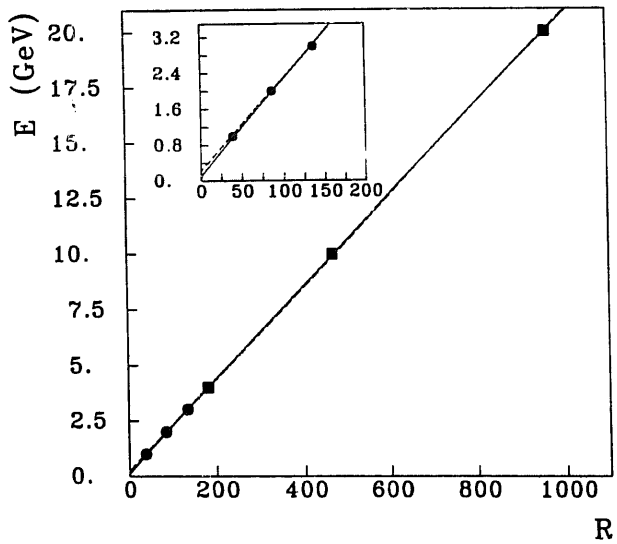

Fig. 8. Energy response R of a lead-glass cluster with up to nine modules deduced from DESY (solid circles) and CERN-SPS (solid squares) calibration experiments. The solid line represents the power law used in the analysis. The dashed line represents a linear fit for comparison.

in a 10 GeV/c electron beam positioned at the module center. In addition, data were taken with 4 and 20 GeV/c electrons and, in order to investigate the response to hadronic showers and minimum ionizing particles, with a mixed hadron beam (protons and π). Electron beams available at DESY allowed to investigate the low-energy calibration curve down to 1 GeV/c for a subset of modules.

The energy calibration function, after correction of the PM nonlinearities, turned out to deviate slightly from a linear behaviour (fig. 8), which is mainly induced by light absorption and threshold effects. The calibration data (symbols) could be well parameterized by an empirical power law (solid line) of the form

$$E = aR^{1-\delta} + b, \qquad (4)$$

with $\delta = 0.0215$, $a = 24.03$ MeV and $b = 100$ MeV. R is the sum of the ADC channel numbers within a shower, which is assumed to reflect the light output seen by the photomultipliers. For comparison, a linear fit with parameters $\delta = 0$, $a = 20.65$ MeV and $b = 228$ MeV is shown in fig. 8 (dashed line), which differs mainly in the very low energy region from the power law fit used in the data analysis.

It turned out that the offset b is rather insensitive to the calibration data. Therefore, refinements have been made by use of the π^0 invariant mass spectra. Further details will be discussed in section 6.2.3.

4.1. Energy resolution

Electromagnetic showers were found to spread over up to 15 modules with a light distribution depending

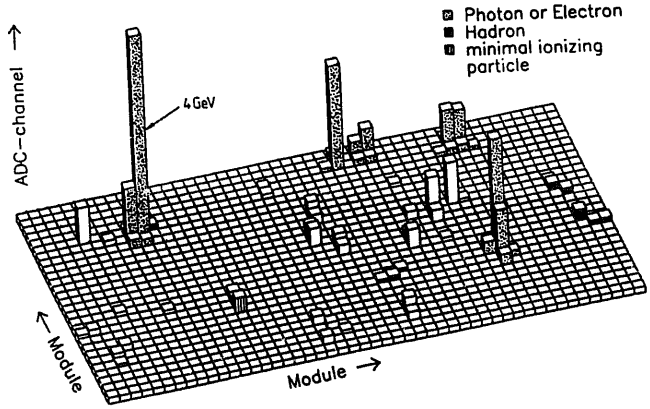

Fig. 9. ADC pulse height distributions in the SAPHIR module array for one single event from a central 200 AGeV $^{16}O+Au$ reaction for electromagnetic and hadronic showers.

strongly on the hit position relative to the module boundaries as well as on the angle of incidence. For perpendicular incidence into the center of the module, 80% of the energy is contained in the hit module itself, decreasing to about 40% for the marginal positions. Typical distributions of the shower light are shown in fig. 9. The shape of this distribution depends only weakly on the energy E of the incident particle. E is calculated from the sum of the signals with a resolution of

$$\frac{\sigma}{E} = 0.4\% + \frac{6\%}{\sqrt{E/\mathrm{GeV}}}, \tag{5}$$

which reveals the dominant influence of the Poisson law for photon number fluctuations via the energy dependence.

Fig. 10 shows spectra of electromagnetic and hadronic showers and minimum ionizing particles. Since the depth of lead glass corresponds to only one interaction length for hadrons, their shower signals fluctuate strongly and are in general much lower than the signals obtained from electromagnetic showers. The pulse height generated by minimum ionizing particles is equivalent to a photon shower of about 540 MeV.

4.2. Position resolution

The fine segmentation of the lead glass allows to obtain the position of incidence from the light distribution in the involved modules. This calculation is done in the following steps:

The center of gravity of the pulse height distribution (x_p) is computed. This is a biased estimate of the actual center of gravity of the shower (x_{rec}), because the modular structure of the detector is folded in. The relation between x_p and x_{rec} can be approximated as:

$$x_{rec} = a_1 \operatorname{arsinh}\left(\frac{x_p}{a_2}\right) \tag{6}$$

for perpendicular incidence, as was already pointed out in ref. [16]. This relation was verified with the data taken in the calibration experiment, where the position of incidence, x_{inc}, was measured with a delay-line wire chamber [17] in front of the detector. The parameter a_1, which is an effective width parameter of the one-dimensional lateral shower distribution [16,18], increases with shower energy (see table 1). The shape of the pulse height distribution is therefore not independent of energy. The corrected center of gravity was then used to estimate the position resolution of the detector. Results are shown in fig. 11 and are also listed in table 1. Since the beam collimator was set to a larger opening for the

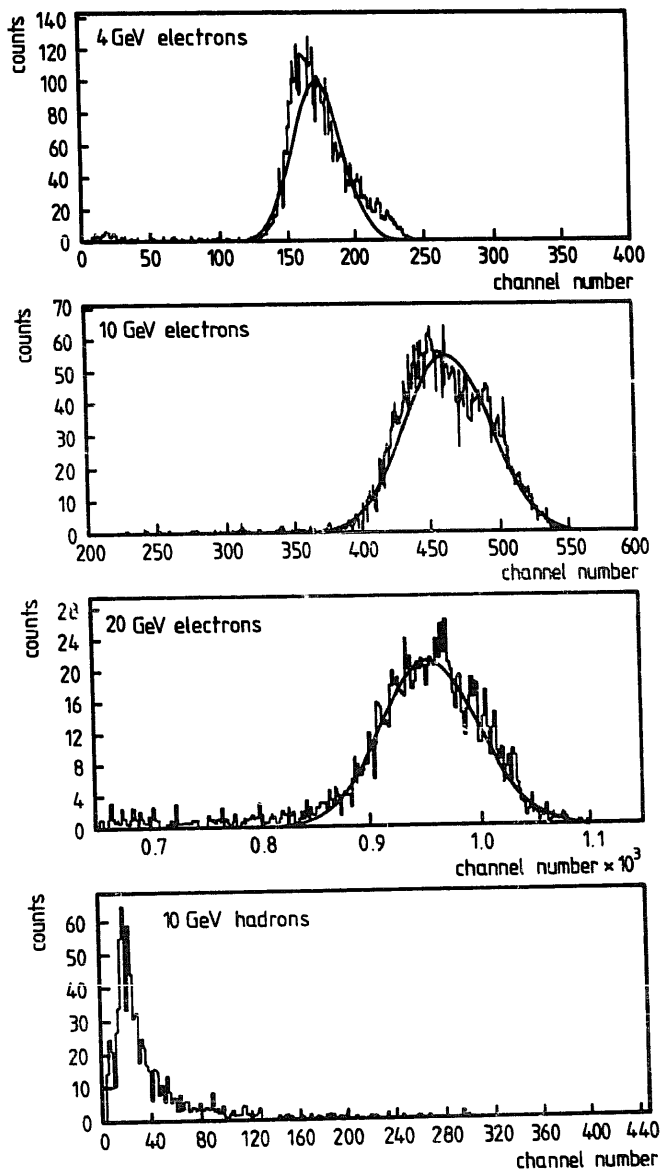

Fig. 10. Energy spectra generated from the sum of pulse heights in one central and eight adjacent detector modules for 4, 10 and 20 GeV electrons and 10 GeV hadrons with the peak introduced by minimum ionizing particles.

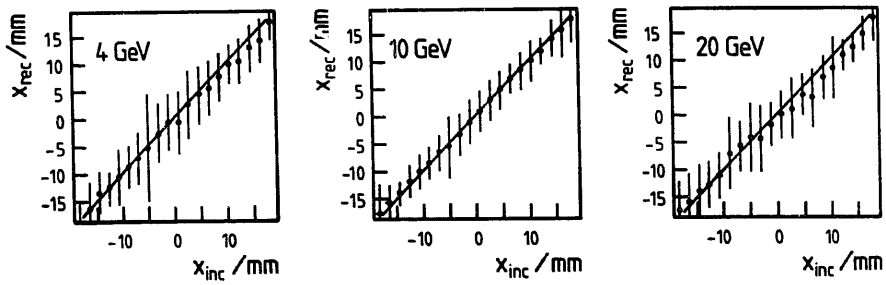

Fig. 11. True (x_{inc}) versus estimated (x_{rec}) position of hits of electrons with different energies.

Table 1
Effective shower width and position resolution

p [GeV/c]	a_1 [mm]	σ_x [mm]
4	5.8	4.7
10	6.4	3.3
20	7.4	4.4

4 and 20 GeV/c beams, the position of incidence was not so well defined in these cases, and this fact slightly worsened the apparent position resolution.

For the needs of the WA80 experiment the correction function (eq. (6)) could be generalized for nonperpendicular incidence. Taking into account the position offset between the center of gravity x_{rec} and the point of impact x_{inc}, the position can be obtained from the function

$$x_{rec} = a_1 \operatorname{arsinh}\left(\frac{x_p - a_3}{a_2}\right) + a_4, \qquad (7)$$

using the first moment x_p of the pulse height distribution. The detailed angular dependence was studied with a shower parameterization [19]. The a_i appear to be smoothly varying functions of the angle of incidence. We obtained a position resolution of 5 mm for an angle of incidence of 15° at 10 GeV/c. In the actual data processing eq. (7) is used as a starting point, and the final position value is then found by fitting a simulated shower light distribution to the measured shower. This fitting is also part of the particle identification algorithm (see section 6.1).

5. Charged-particle veto

The photon identification is complicated by the presence of numerous charged particles at midrapidity (mostly pions). Minimum ionizing particles may mimic low-energy photons, and the strong statistical fluctuations of hadronic showers are capable to fake an electromagnetic shower with a certain probability even in only one hadronic interaction length. Thus a tag for charged particles hitting the surface of SAPHIR is needed.

Table 2
SAPHIR construction items and performance

Material	1278 lead-glass modules SF5
Module cross section	35×35 mm^2
Module length	460 mm ≡ 18 radiation lengths (98% containment for 30 GeV photons)
Total (rectangular) area	98×171.5 cm^2
Energy resolution	$\sigma_E = E(6/\sqrt{E/\text{GeV}} + 0.4)\%$
Spatial resolution	$\sigma_x \leq 3$ mm for perpendicular incidence $\sigma_x \leq 4$ mm for 15° inclined incidence
Gain stability	$(0.5 \pm 0.6)\%$
Dynamic range	50 MeV to 25 GeV
Minimum ionizing signal	540 MeV photon equivalent

This task is accomplished by two layers of Iarocci-type plastic streamer tube arrays (LAM1 and LAM2) of the coverless design [20] with pad readout [21]. The planes are located 2.4 and 2.65 m from the target and cover SAPHIR completely. The pad sizes of LAM1 and LAM2 are 2.1×5.2 and 5.2×3.5 cm^2 depending on the pseudorapidity region, i.e. on the particle density, and are furthermore reduced to 1.0×2.6 cm^2 in the overlap region of LAM2 with SAPHIR. Fired pads with common border lines are grouped into a cluster of pads which is called a *hit*. The position of a hit is calculated as the center-of-gravity of this cluster. The overall detection efficiency for a single layer is about 85% (92% would be the geometrical limit) and hence ≈ 98% for a logical or of the two layers.

Each hit is projected, assuming the origin of the particle in the target, onto the front surface of SAPHIR and the corresponding lead-glass module is marked by a charged particle veto flag. In the following analysis a detected hit in this module and in its neighbours is considered not to be a photon. In fig. 12 energy spectra of photons and charged particles from 200 A GeV ^{16}O + Au reactions are presented which clearly show the

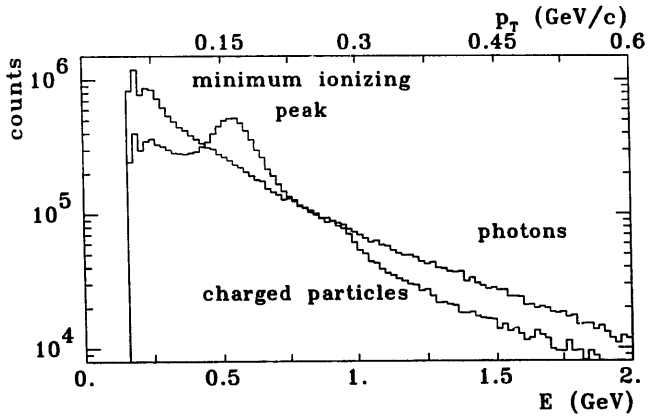

Fig. 12. Energy spectra of photons and charged particles for 200 AGeV $^{32}S+Al$. In addition to the (kinetic) energy scale, an estimate of the corresponding transverse-momentum scale is given.

minimum ionizing peak at 540 MeV photon equivalent energy in the charged-particle spectrum. The misidentification of photons due to an accidental nearby charged particle hit will be discussed in section 6.3.

6. Photon and π^0 reconstruction

6.1. Photon identification

As mentioned above, electromagnetic showers deposit their energy into more than one module depending on energy, angle of incidence and hit position relative to the module boundaries. Such an area of adjacent modules with a photomultiplier signal above the threshold is called a *cluster*. Each event was analyzed in the following way:

- The pulse height distribution is subdivided into clusters;
- Clusters are classified as charged or neutral hits according to the assignment made by the charged-particle veto detector;
- If a cluster consists of at least three modules, its pulse height distribution is compared with that of a calculated model shower by means of a χ^2 test. This procedure allows to distinguish a single electromagnetic shower from a hadronic one and from the overlap of two showers of any combination (hadronic and electromagnetic).

In the fitting algorithm a combination of a gradient search and a parabolic extrapolation of χ^2 [22] was applied. A parameterization for electromagnetic showers [19] was used to calculate the response of a photon and was found to be valid in comparing the calculation with the energy deposition of electrons from the calibration runs. The small difference between showers initiated by a photon or by an electron has been neglected. The method to determine the photon reconstruction probability will be described in section 6.3.

6.2. Reconstruction of the π^0 and η transverse-momentum distribution

6.2.1. Neutral meson decay

The pseudoscalar π^0's and η's decay isotropically in their rest frames into two photons with a branching ratio of $98.8 \pm 0.03\%$ and $38.9 \pm 0.4\%$, respectively [23]. Due to the short lifetime of 0.84×10^{-16} and 0.61×10^{-18} s, respectively, they decay unmeasurably close to the target. According to energy and momentum conservation, the two decay photons fulfill the following equation in the laboratory system:

$$M = \sqrt{2E_1E_2(1-\cos\psi)}\,, \tag{8}$$

M = meson rest mass,
E_1, E_2 = energies of photon 1 and 2,
ψ = opening angle between decay photons.

As will be discussed later, the condition imposed by eq. (8) is necessary but not sufficient to select photons resulting from an actual meson decay. With SAPHIR we are measuring π^0's in the momentum range from 2 to 16 GeV/c. According to the Lorentz boost of the decay photons along the π^0 direction, the opening angle ψ for most π^0 decays is less than 10° in the laboratory system.

6.2.2. Geometrical acceptance

Because of SAPHIR's limited solid angle, the probability to detect both decay photons of those mesons emitted into its solid angle is smaller than 1. In order to investigate the dependence of the geometrical acceptance on the π^0 and η momentum and emission angle, a Monte Carlo simulation was carried out. In the laboratory system the inclusive azimuthal distribution for a large number of events is uniform. This is true even if there would be an azimuthal structure in single events. As a consequence, a uniform distribution for the π^0 and η azimuthal angle ϕ was used in the Monte Carlo calculation. In fig. 13 the geometrical acceptance averaged over $\phi(\pi^0)$ is shown as a function of the π^0 transverse momentum and the cosine of the π^0 polar angle θ. In this calculation a software energy-threshold of 500 MeV was applied to the decay photons. At very low transverse momenta ($p_T < 0.4$ GeV/c) the geometrical acceptance is negligibly small due to either the energy threshold for photons or the large opening angle ψ between the decay photons. Going to higher π^0 p_T values, the acceptance increases until the merging of two π^0 decay photons into one single shower appears at a $p_T(\pi^0) \approx 4$ GeV/c. In order to determine the one-dimensional π^0 and η p_T acceptance shown in fig. 14, the two-dimensional acceptance was integrated over the θ

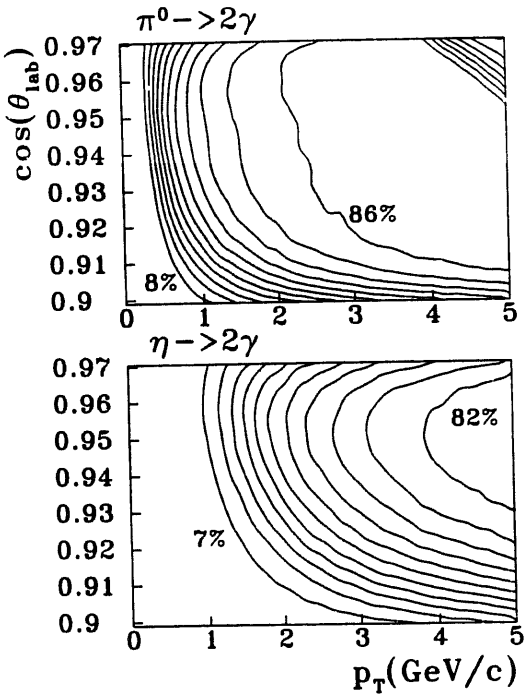

Fig. 13. Geometrical acceptance of SAPHIR for π^0 and η as a function of p_T and cos θ. The values are averaged over all ϕ angles. A lower cut of 500 MeV was applied to the photon energy. The contour lines have a linearly equidistant spacing.

angle using a realistic θ distribution as a weighting function. The θ distribution from the event generator FRITIOF [24] was applied here. The assumption made by this procedure is that the p_T and θ distributions are uncorrected. This is fairly well fulfilled in SAPHIR's solid angle [25]. The sensitivity to the energy threshold for the acceptance calculation is analyzed by varying the energy threshold by σ_E (500 MeV) $\approx$ 50 MeV and is shown by the shaded area in fig. 14.

An independent way to check the reliability of the acceptance calculation is to compare distributions of the energy asymmetry α:

$$\alpha = \frac{|E_1 - E_2|}{E_1 + E_2}, \tag{9}$$

where E_1, E_2 are decay photon energies, from experimental data with those from the Monte Carlo calculation.

Fig. 15 shows results for peripheral and central 200 A GeV $^{16}O + Au$ collisions. The distributions agree within the statistical errors with the Monte Carlo calculations. Hence it can be concluded from the region $\alpha > 0.5$ that the detector geometry and energy cut is well implemented in the Monte Carlo simulation, and from the region $\alpha < 0.2$ that the merging of decay photons does not occur in the p_T region under consideration.

6.2.3. π^0 and η meson identification

In order to identify π^0 and η mesons all photon pair combinations are used to calculate the invariant mass in each event. Fig. 16 displays an invariant mass spectrum for events with a multiplicity of two or three photons. Both, the π^0 and η can clearly be observed in this spectrum. However, according to SAPHIR's acceptance the π^0 peak is easier to identify than the η peak. In fig. 17 invariant mass spectra for different bins of transverse momentum $p_T(\gamma, \gamma)$ are plotted. Fitting a third-order polynomial to the combinatorial background and subtracting this background from the mass spectrum

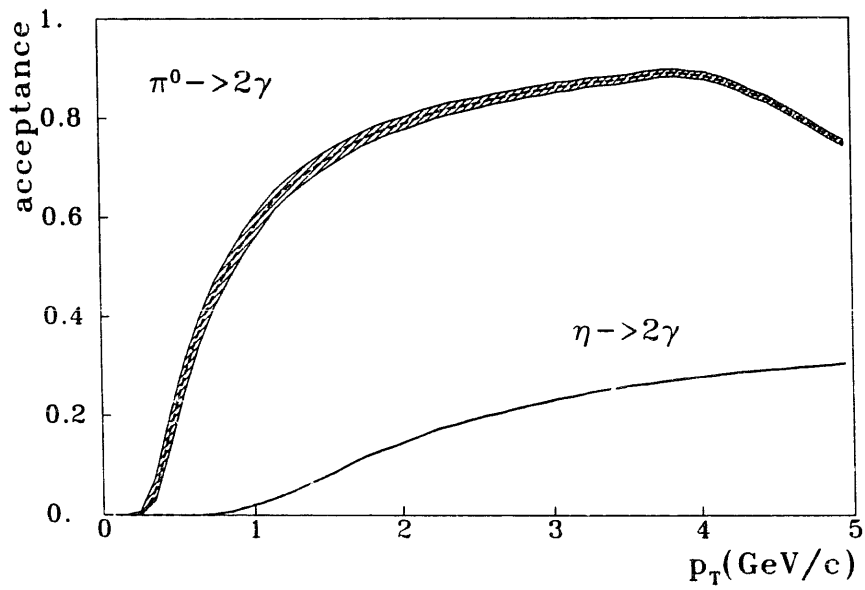

Fig. 14. Geometrical acceptance of SAPHIR for π^0 and η as a function of p_T, averaged over both ϕ and θ angles. The shaded area corresponds to a variation of 50 MeV for the energy cut.

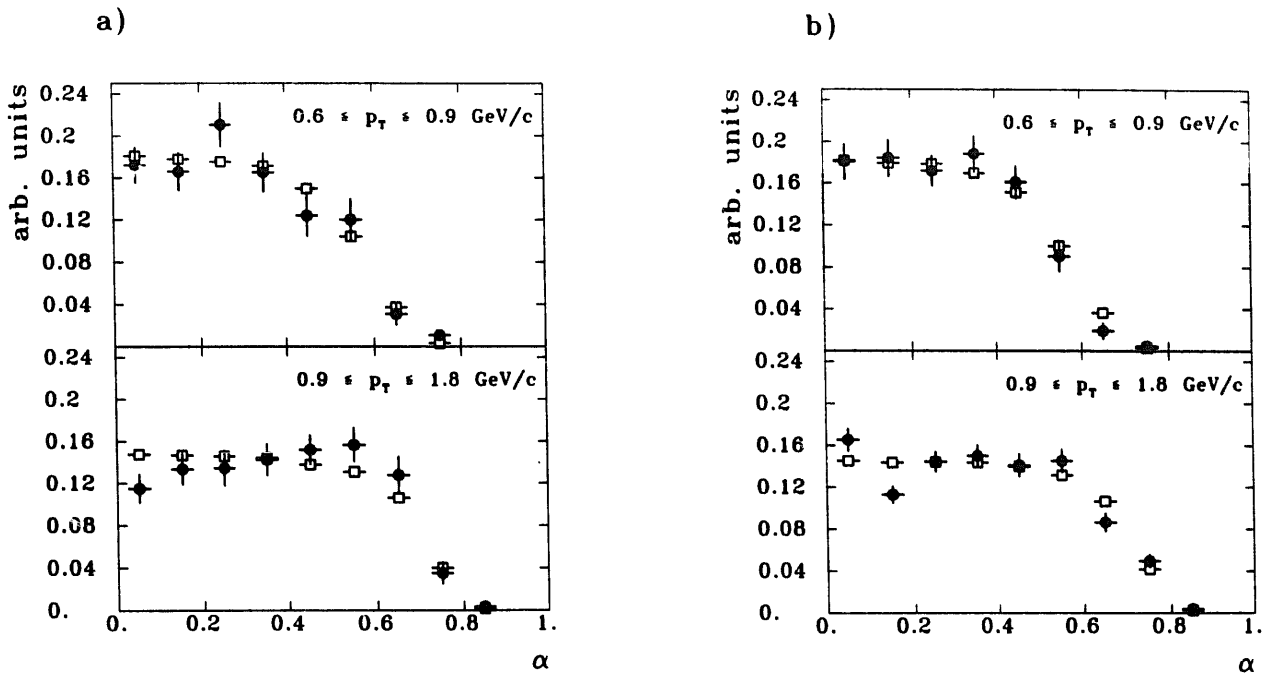

Fig. 15. Energy asymmetry α (solid circles) for (a) peripheral and (b) central 200 AGeV ^{16}O+Au events for two p_T regions. For comparison the Monte Carlo results are shown (□).

yields the number of π^0 mesons measured in the corresponding p_T bin. The π^0 peak area is integrated from 107 to 167 MeV/c^2 which corresponds to 99.7% of the area assuming a Gaussian function with a σ of 10 MeV/c^2. The uncertainty σ_N in determining the number N of neutral pions in a p_T bin is determined by the statistics and the peak to total ratio Q:

$$\sigma_N = \sqrt{\frac{2N}{Q} - N}\,. \tag{10}$$

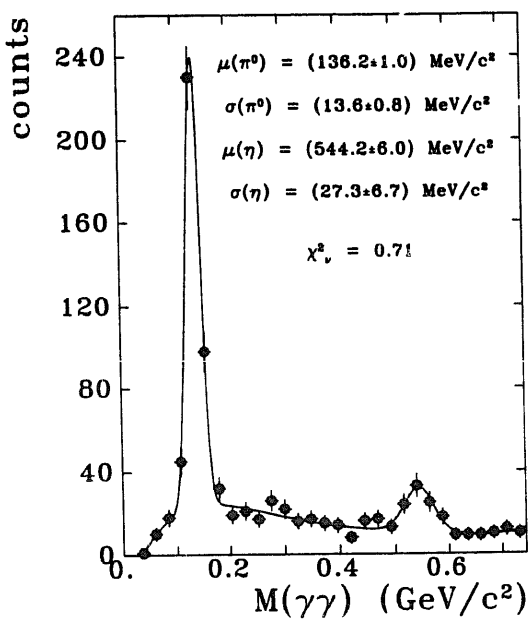

Fig. 16. Invariant mass spectra from events with two or three photons and the sum of the photon energies above 8 GeV.

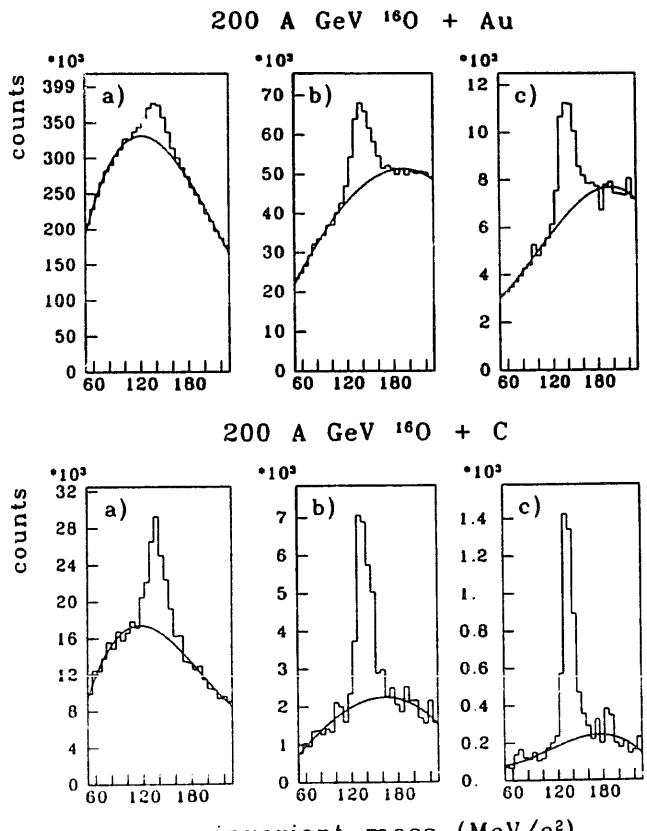

Fig. 17. Invariant mass spectra of γγ pairs for ^{16}O+Au and ^{16}O+C at 200 AGeV in different regions of transverse momentum $p_T(\gamma, \gamma)$: (a) $0.4 \le p_T \le 0.8$ GeV/c, (b) $0.8 \le p_T \le 1.2$ GeV/c, (c) $1.2 \le p_T \le 1.6$ GeV/c. Only photons with $E_\gamma > 500$ MeV are considered.

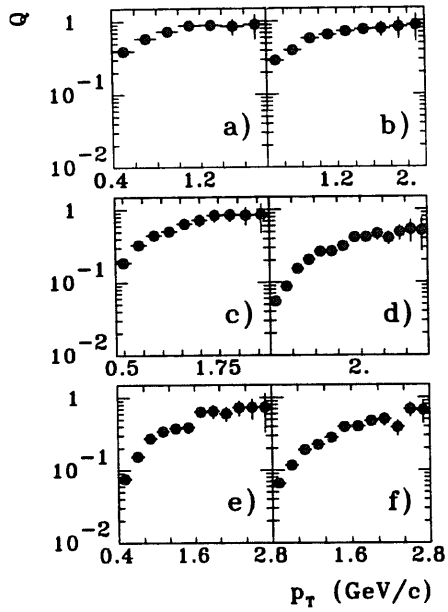

Fig. 18. Signal-to-total ratio Q for the π^0 mass as function of p_T for the following systems: (a) 200 GeV p+C, (b) 200 GeV p+Au, (c) 200 AGeV ^{16}O+C, (d) 200 AGeV ^{16}O+Au, (e) 200 AGeV ^{32}S+Al, (f) 60 AGeV ^{16}O+Au. The mass region from 107 to 167 MeV/c^2 is considered for Q.

In fig. 18 Q is plotted as a function of $p_T(\pi^0)$ for different reaction systems. For all systems Q increases with increasing $p_T(\pi^0)$, i.e. the quality in determining the number of π^0's improves. The comparison of the peak-to-total ratios Q obtained from 200 GeV p + C and 200 AGeV ^{16}O + Au events (fig. 18a, d) reveals that Q decreases with increasing cluster multiplicity. The mean cluster multiplicities are 1.5 and 11.2, respectively. In addition, Q reflects the probability to identify a π^0 on an event-by-event basis.

Next, the π^0 transverse-momentum distribution has to be corrected for the p_T acceptance to obtain a π^0 p_T spectrum emitted into SAPHIR's solid angle. This analysis technique has been extensively tested by using the event generator HIJET [26] as a π^0 source and applying SAPHIR's geometry, energy and position resolution to the Monte Carlo data [27].

Of primary interest for the physical analysis are the resolutions of $p_T(\gamma)$, $p_T(\pi^0)$ and of the invariant mass M of photon pairs, which can be expressed in terms of the energy and position resolution. The resolution in $p_T(\gamma)$ can be calculated using error propagation:

$$\frac{\sigma_{p_T}(\gamma)}{p_T(\gamma)} = \sqrt{\left(\frac{\sigma_E}{E}\right)^2 + \left(\frac{\sigma_\theta}{\tan\theta}\right)^2}. \qquad (11)$$

σ_θ varies from 1.43×10^{-3}–1.41×10^{-3} and can therefore be neglected. The dominant contribution to the error is due to the energy resolution. The resolution σ of the estimate μ for the invariant mass M can be expressed as follows:

$$\frac{\sigma}{\mu} = \sqrt{\left(\frac{\sigma_{E_1}}{2E_1}\right)^2 + \left(\frac{\sigma_{E_2}}{2E_2}\right)^2 + \left(\frac{\sigma_\psi}{2\tan(\psi/2)}\right)^2}. \qquad (12)$$

Eq. (12) offers the possibility to examine whether the energy and position resolutions derived from the calibration data still hold in a high-multiplicity environment, i.e., for heavy-ion reactions. For symmetric ($\alpha = 0$) and asymmetric ($\alpha = 0.6$) decays fig. 19 displays, as a solid and dashed line, the calculated invariant mass

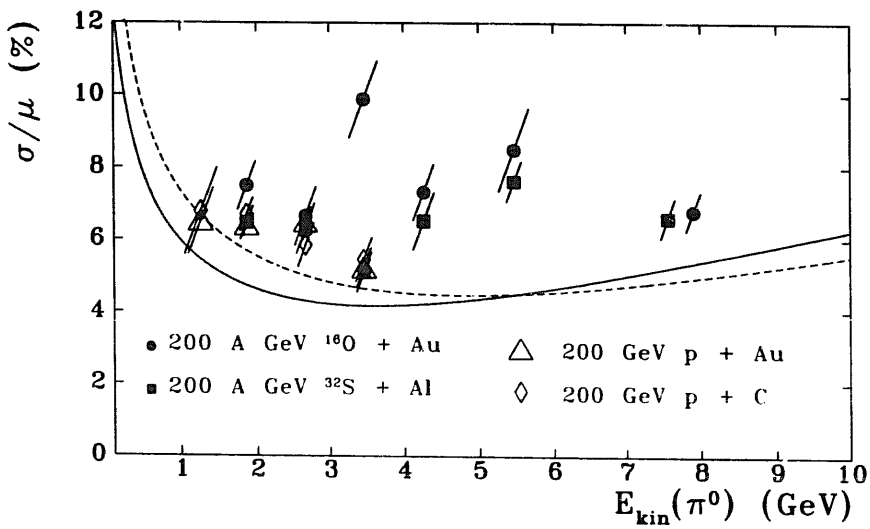

Fig. 19. Resolution of the invariant mass calculated from the energy and position resolution as measured in the calibration experiments compared to the values obtained from proton and heavy-ion induced data. The calculation is shown as a function of the kinetic energy of the π^0 for a symmetric (solid line) and an asymmetric ($\alpha = 0.6$, dashed line) π^0 decay. The experimental data are obtained for the symmetric decay using a Gaussian and polynomial function for the fit to the mass spectra.

resolution using eq. (5) for the energy resolution and the following parameterization for the position resolution:

$$\sigma_x = 5\ \text{mm}(E/\text{GeV})^{-0.155} \quad (13)$$

The data points in fig. 19 are extracted for the symmetric π^0 decay by fitting a Gaussian and a polynomial to the mass spectra. All data points are 1–2% above the predicted resolution indicating that in addition to the intrinsic energy and position resolution the problem of overlapping showers worsens the resolution. Assuming the parameterizations from eqs. (5) and (13) an effective energy resolution of $8.6\%/\sqrt{E/\text{GeV}}$ and a position resolution of 8.5 mm $(E/\text{GeV})^{-0.155}$ is obtained by a fit to the experimental data.

The energy calibration function (see eq. (4)) can be checked by investigating the variation of the fitted π^0 peak position μ as a function of the energy of one photon, keeping the other photon energy fixed in a certain energy interval. Any nonlinearity should then be visible as a deviation of μ from the π^0 rest mass. In fig. 20 one photon energy fulfilled the constraint $0.8 \le E_\gamma \le 2$ GeV for the π^0 peak positions μ (solid circles). For all four systems the peak position is nearly constant as a function of photon energy. Using the linear fit of the calibration data instead of eq. (4) would lead to a π^0 peak position μ of approximately 150 MeV/c^2 in fig. 20 at $E_\gamma \approx 0.5$ GeV. This finding obviously prefers eq. (4) and demonstrates that even for low energies the calibration can be fixed precisely. However, the mean peak position varies from 136.6 ± 0.2 MeV/c^2 and 136.2 ± 0.2 MeV/c^2 for 200 GeV p + Au and 200 A GeV ^{16}O + C, respectively, to 138.4 ± 0.3 MeV/c^2 for 200 A GeV ^{16}O + Au. The higher cluster multiplicity for the 200 A GeV ^{16}O + Au events increases the probability that two showers merge to one. This tends to increase the energy of the shower and accounts for a higher mass of the reconstructed π^0 and an asymmetric shape of the mass spectrum. In order to account for this effect, an asymmetric Gaussian with the following parameterization was used:

$$f(x) = \begin{cases} A \exp\left(\dfrac{-0.5\omega^2}{1+\beta\omega}\right) & \text{for } x \ge \mu, \\ A \exp(-0.5\omega^2) & \text{for } x < \mu, \end{cases} \quad (14)$$

$$\omega = \frac{x-\mu}{\sigma}.$$

For the 200 A GeV ^{16}O + Au events these peak positions (○) agree with the π^0 rest mass value above a photon energy of 2 GeV, whereas for lower photon energies this parameterization is not sufficient.

6.3. Photon reconstruction efficiency

The probability that a photon is correctly identified as a neutral particle can be determined by calculating the invariant mass for pairs of one photon, called *trigger particle*, combined with all other particles in the same event. The trigger particles γ_t have been chosen from the neutral electromagnetic particles with an energy above 400 MeV. For a 100% reconstruction probability a π^0 peak should appear only in the mass spectrum filled by the photon–photon combinations. With the very realistic assumption that the photon identification is not biased for the π^0 decay photons, the reconstruction probability ϵ is determined by the

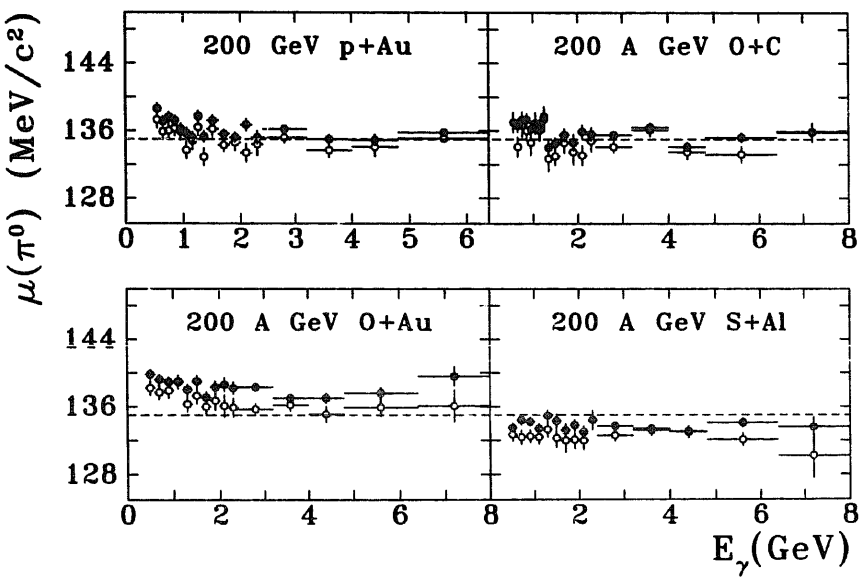

Fig. 20. The position μ of the π^0 peak obtained by fits of a polynomial plus a Gaussian to the mass spectra as a function of the energy of one photon (●). The energy of the other photon is restricted to the energy interval 0.8 GeV $\le E_\gamma <$ 2 GeV. Results obtained by using an asymmetric Gaussian are also shown (○). (For definition see text.)

ratio of π^0 peak areas A taken from the different invariant mass spectra with particle combinations $\gamma_t + \gamma$ particles and γ_t + other particles,

$$\epsilon_\gamma = \frac{A_\gamma}{A_\gamma + A_{\text{other}}}, \tag{15}$$

where A_γ is the π^0 peak area for the combination of γ_t and a neutral electromagnetic particle, and A_{other} is the π^0 peak area for the combination of γ_t and another (not neutral electromagnetic) particle.

In the same way the reconstruction efficiency for other types of particles can be determined. Instead of using the $\gamma_t + \gamma$ particle combinations, we calculated

$$\epsilon_{\text{neutral}} = \frac{A_{\text{neutral}}}{A_{\text{neutral}} + A_{\text{charged}}} \tag{16}$$

from the γ_t + neutral and γ_t + charged particle combinations. This value is more suited for the analysis because of much smaller statistical errors than ϵ_γ. In fig. 21 $\epsilon_{\text{neutral}}$ is shown as a function of the photon transverse momentum for the reaction of 200 GeV p + C and 200 GeV p + Au. Due to material in front of SAPHIR (vacuum chamber, streamer tubes and the target itself), the photons have a total conversion probability of 6% for the Au target. Hence the probability of about 90% determined by this method is close to the upper limit of 94% due to conversion. In other words, 4% of all neutral particles are misidentified as charged ones. This probability can be interpreted as the efficiency of the photon reconstruction if the problem of overlapping showers can be neglected or regarded as a small distortion. In the low-multiplicity environment of p + C and p + Au this condition might be fulfilled, however refined methods are necessary to determine the photon reconstruction efficiency for higher particle densities as those observed in central reactions with ^{16}O and ^{32}S beams. This method will be described in a forthcoming publication.

7. The high-energy photon trigger

In order to enhance the data sample of events with high transverse-momentum photons, a special trigger setup has been developed. It recognizes a high signal in one of the SAPHIR lead-glass modules which indicates a high-energy photon hitting the detector. The trigger is derived from the ninth dynode of the ten-stage photomultiplier which is accessible via a transformer, and the signal of each photomultiplier dynode is analyzed by an individual discriminator. The output signals of all discriminators are summed up with a contribution of 100 mV per fired discriminator, allowing to distinguish numbers of fired discriminators up to 50 in an output range of 5 V. In the present trigger setup this information has not been used because one fired discriminator was considered sufficient to flag an interesting event. Since the events should be selected for high transverse momentum rather than high energy, the settings of the discriminator thresholds depend on the laboratory angles of the individual modules. Furthermore, the relative gain of the anode and dynode signal varies significantly because the voltage dividers of the photomultipliers were trimmed differently in order to achieve a minimum deviation from a linear anode response over a wide dynamic range. Before the assembly of SAPHIR, all photomultipliers have therefore been tested and selected in three groups of different dynode output values with an overall variation of at most ±20% within one group. Since 48 discriminators are mounted in one housing with a common threshold level supply, clusters of 48 modules with similar dynode signals and not significantly different laboratory angles are connected to one discriminator unit.

In order to determine the efficiency of the trigger electronics flagging high transverse-momentum photons, the particle with the highest p_T has been selected from each event. Since we cannot tell which particle actually caused the trigger in a given event, we assume

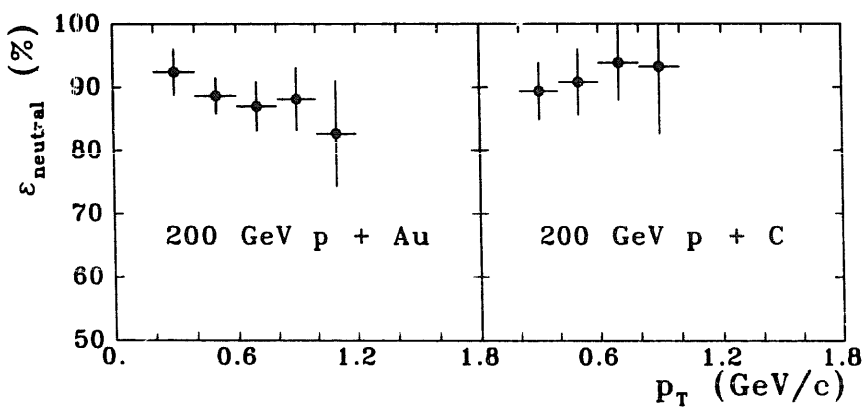

Fig. 21. Photon reconstruction probability as a function of $p_T(\gamma)$ for minimum bias p + C and p + Au at 200 GeV.

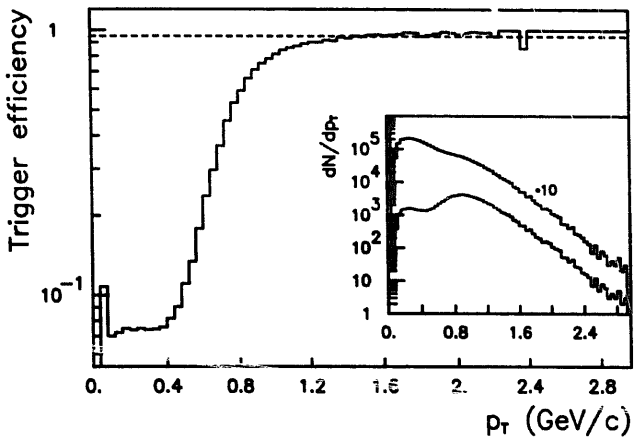

Fig. 22. The ratio of the highest transverse-momentum photons from events flagged by the high p_T trigger and from all recorded events, showing the efficiency of the high transverse-momentum photon detection. The horizontal dashed line indicates the 95% level. The inset shows the original distributions for 200 A GeV ^{32}S + Al.

that this highest p_T particle was responsible for the trigger. For the 200 A GeV ^{32}S + Al system, we analyzed the p_T distributions of the highest transverse-momentum photons from all events recorded and from those events flagged by the high p_T trigger. With a particle above the p_T threshold present, the event should have been flagged by the high p_T trigger, and the ratio of the distributions should become 1 above the threshold. The ratio of the distributions is shown in fig. 22, the horizontal dashed line indicating the 95% level. The inset shows the distributions of the highest transverse-momentum photons. The efficiency is 90% at the threshold value of 1.2 GeV/c and better than 95% above 1.5 GeV/c.

These values do not yet give information about the true enhancement of high p_T photons achieved by the high p_T trigger. To calculate this, one has to take into account that a fraction of the events flagged by the high p_T trigger would have been recorded anyhow because one of the other triggers fired simultaneously. For each possible combination of triggers this fraction was calculated and the number of events from a given combination was scaled accordingly. In this way, the photon spectrum as it would have been measured without the high p_T trigger could be constructed and compared to what was actually recorded. The result is shown in fig. 23. On the average, the photon statistics in the high p_T tail above 1.2 GeV/c is enhanced by a factor of 6.

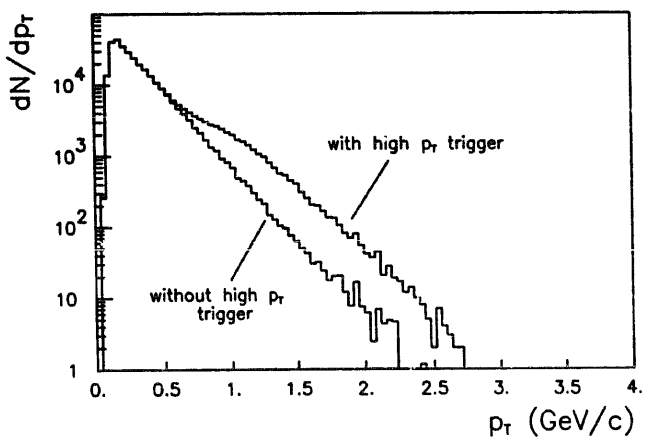

Fig. 23. The enhancement in the high p_T tail of the photon transverse-momentum spectra due to the high p_T trigger for the 200 A GeV ^{32}S + Al system.

Acknowledgements

We thank our mechanical and electronic workshop for their competent work and continuous help during the construction and the assembly of the SAPHIR detector.

This work has partly been funded by the Federal Minister for Research and Technology (BMFT) under contract number 06 MS 984 and by the GSI.

References

[1] H. Satz, H. Specht and R. Stock (eds.), Proc. Sixth Int. Conf. on Ultra-Relativistic Nucleus–Nucleus Collisions, Z. Phys. C38 (1988).

[2] A. Bamberger et al., NA35 Collaboration, Phys. Lett. B184 (1987) 271.

[3] R. Albrecht et al., WA80 Collaboration, Phys. Lett. B199 (1987) 297.

[4] J. Schukraft, Proc. Seventh Int. Conf. on Ultra-Relativistic Nucleus–Nucleus Collisions, 89–91, Nucl. Phys. A498 (1989) 89 and references therein.

[5] M. Jacob and H. Satz (eds.), Quark Matter Formation and Heavy Ion Collisions, Proc. Bielefeld Workshop, May 1982 (World Scientific, 1982).

[6] R.C. Hwa and K. Kajantie, Phys. Rev. D32 (1985) 1109; S. Raha and B. Sinha, Phys. Rev. Lett. 58 (1987) 101.

[7] R. Albrecht et al., WA80 Collaboration, Phys. Lett. B201 (1988) 390.

[8] K.S. Lee and U. Heinz, Z. Phys. C43 (1989) 425.

[9] H.H. Gutbrod et al., Study of relativistic nucleus–nucleus collisions at the CERN-SPS, GSI preprint GSI-85-32, August 1985 and CERN SPSC/85-39/M406.

[10] F. Binon et al., Nucl. Instr. and Meth. 188 (1981) 507.

[11] Phototube manufactured by Philips–Valvo, 11/8 in. tube diameter, tube coated with conductive paint and connected to cathode potential, 10 dynode stages, gain $\approx 10^6$, S11 type photocathode with 23 mm diameter.

[12] ^{241}Am-doped NaI crystal of 0.2 cm^3 produced by Harshaw Chemical Company, USA. Light output equivalent to 4 MeV γ energy, count rate 100 and 1000 counts/s; respectively.

[13] LN100 nitrogen laser produced by PRA Laser Inc., Canada; pulse width 300 ps, pulse energy 75 μJ, wavelength 337 nm.
[14] Step index multimode plastic clad silica optical fibre, produced by Fibre Optiques Industries, France; PCS200 with (200±8) μm core diameter and 0.1 dB/m attenuation measured at 420 nm; PCS1000 with (1000±40) μm core diameter and 0.15 dB/m attenuation measured at 337 nm.
[15] M. Kobayashi, S. Takano and Y. Matsumoto, Nucl. Instr. and Meth. 224 (1984) 318.
[16] G.A. Akopdjanov et al., Nucl. Instr. and Meth. 140 (1977) 441.
[17] A. Manarin and G. Vismara, The delay wire chamber description, LEP/BI-TA/Note 85-3, Prévessin (1985).
[18] T. Peitzmann, Diploma Thesis, Münster (1987).
[19] M. Della Negra, Phys. Scripta 23 (1981) 469;
E. Longo and I. Sestili, Nucl. Instr. and Meth. 128 (1975) 283.
[20] E. Iarocci, Nucl. Instr. and Meth. 217 (1983) 30.
[21] R. Albrecht et al., WA80 Collaboration, Nucl. Instr. and Meth. A276 (1989) 131.
[22] P.R. Bevington, Data Reduction and Error Analysis for the Physical Sciences (McGraw-Hill, 1969).
[23] Review of Particle Properties, Phys. Lett. B204 (1988).
[24] B. Nilsson-Almqvist and E. Stenlund, Comp. Phys. 43 (1987) 387;
B. Andersson et al., Nucl. Phys. B128 (1987) 289.
[25] H. Löhner et al., WA80 Collaboration, Z. Phys. C38 (1988) 97.
[26] T. Ludlam, Study of high energy densities over extended nuclear volumes via Nucleus-Nucleus collisions at the SPS, NA34, CERN-SPS/84-43, SPSC/P203 (1984);
T. Ludlam et al., RHIC Workshop I, eds. P. Haustein and C. Woody, Brookhaven, April 1985, BNL-51921.
[27] L. Dragon, Diploma Thesis, Münster (1985);
S. Sørensen, Nucl. Phys. A461 (1987) 487c.